



Enhanced activity of microwave synthesized hierarchical MnO_2 for high performance supercapacitor applications

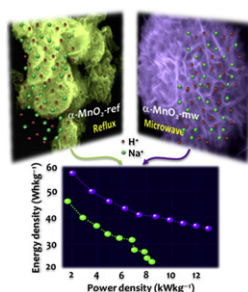
Sumanta Kumar Meher, G. Ranga Rao*

Department of Chemistry, Indian Institute of Technology Madras, Chennai 600 036, India

HIGHLIGHTS

- ▶ $\alpha\text{-MnO}_2$ samples were synthesized using microwave-assisted and reflux methods.
- ▶ Microwave synthesized $\alpha\text{-MnO}_2$ shows higher rate pseudocapacitance.
- ▶ Microwave synthesized $\alpha\text{-MnO}_2$ shows lower ESR, IR drop and capacitance retention.
- ▶ Microwave synthesized $\alpha\text{-MnO}_2$ shows high power and energy density.

GRAPHICAL ABSTRACT



ARTICLE INFO

Article history:

Received 7 February 2012

Received in revised form

23 April 2012

Accepted 27 April 2012

Available online 18 May 2012

Keywords:

Manganese oxide
Microwave synthesis
Supercapacitor
Energy storage
Energy density

ABSTRACT

In this study, exclusive affect of microwave mediated synthesis on the physicochemical and electrochemical properties of $\alpha\text{-MnO}_2$ have been differentiated from that of $\alpha\text{-MnO}_2$ synthesized in conventional-reflux method. The TG, XRD, BET and SEM analyses show improved physicochemical properties like additional lattice K^+ ions, better crystallinity, high surface area ($155 \text{ m}^2 \text{ g}^{-1}$) as well as pore volume ($0.67 \text{ cm}^3 \text{ g}^{-1}$) and hierarchical porous ball-like morphology of the microwave-synthesized $\alpha\text{-MnO}_2$. The CV studies show lower polarization resistance and higher rate pseudocapacitance (258 Fg^{-1} at 100 mVs^{-1}) of microwave-synthesized $\alpha\text{-MnO}_2$ as compared to its reflux-synthesized counterpart (168 Fg^{-1} at 100 mVs^{-1}). The CP studies show better high rate charge-discharge performance (146 Fg^{-1} at 16 Ag^{-1}), longer cyclic stability (91.4% capacitance retention after 400 charge-discharge cycles at 16 Ag^{-1}) and higher Coulombic efficiency ($\sim 100\%$) of microwave-synthesized $\alpha\text{-MnO}_2$ as compared to the reflux-synthesized sample (80 Fg^{-1} at 16 Ag^{-1} ; 74.1% capacitance retention after 400 charge-discharge cycles at 16 Ag^{-1} ; 85% Coulombic efficiency). Further, due to facile mass transfer in the perfectly porous matrix, the microwave-synthesized $\alpha\text{-MnO}_2$ shows lower equivalent series resistance and better frequency response (higher specific capacitance at elevated operating frequency) as revealed from the impedance studies.

© 2012 Elsevier B.V. All rights reserved.

1. Introduction

Development of sustainable and renewable energy future has been the most important challenge for scientists and engineers

internationally, for addressing the rapidly depleting fossil fuels [1]. In this context, supercapacitors comprising a characteristic combination of high power and reasonable energy density with faster response time and near-infinite life cycle in a wide operational temperature range, can complement other energy storage devices like conventional capacitors, batteries and fuel cells [2–8]. High surface area carbon, polymers and transition metal oxides are the arrays of efficient electrode materials exploited for capacitive

* Corresponding author. Tel.: +91 44 2257 4226; fax: +91 44 2257 4202.
E-mail address: grrao@iitm.ac.in (G.R. Rao).

(charge separation at electrode–electrolyte interface; non-Faradaic) and pseudocapacitive (reversible redox reaction; Faradaic) Among these potential materials, much effort has been devoted to improve the power and energy densities of transition-metal oxides due to their low cost as well as high specific capacitance, originated from variable oxidation states and multi-electron transfer during redox transitions within the potential range of water decomposition [2–11]. Various forms of RuO_2 and hydrous RuO_2 are found to be remarkable in supercapacitor applications due to their ultrahigh theoretical capacitance ($\sim 2000 \text{ Fg}^{-1}$) in a wider applied potential window of $\sim 1.4 \text{ V}$, higher room temperature electrical conductivity and significant chemical and thermodynamic stability under the usual electrochemical environment [9–12]. However, toxicity and expensiveness are the major shortcomings of RuO_2 for its widespread commercial applications. Among the other transition-metal oxides, different crystallographic forms of MnO_x are identified as better materials for supercapacitor applications due to their abundance, superior environmental benignity and high structural flexibility along with suitable physical and efficient electrochemical properties [13–15]. Among various crystallographic structures of MnO_x , $\alpha\text{-MnO}_2$ is recognized as the most favorable for supercapacitor applications due to its wide tunnel size ($\sim 4.6 \text{ \AA}$) and large specific surface area [16]. It has been established that the energy storage in MnO_2 based supercapacitors can be capacitive as well as pseudocapacitive [17–19]. Therefore, to achieve fast capacitive response and high volumetric capacitance, open nanoscale porosity in the MnO_x matrix is especially important for superior accessibility by the electrolytes to enhance the interfacial area for electron/ion adsorption and unhindered mass transport during reversible redox reaction process. In addition, improving the rather poor electrical conductivity (10^{-5} – 10^{-6} Scm^{-1}) and structural stability as well as flexibility for better electronic/ionic conductivity and long-term electrochemical cyclability are some of the foremost challenges in improving the efficiency of MnO_2 [20]. In this context, hierarchical $\alpha\text{-MnO}_2$ with highly synergic nanometer-sized building blocks and micrometer-sized infinite variety of structures have been widely reported in the literature for high performance supercapacitor applications [13–15,21–29]. However most of the reported synthesis methods are either hydrothermal mediated [21,27,30] or tedious and expensive combinations of procedures such as use of templates [24,31], noble metals [20,32] and electrochemical deposition [23,25,33] are employed to generate bulk nanostructures and films of $\alpha\text{-MnO}_2$ for supercapacitor applications. Although hydrothermal conditions, due to easily controllable parameters, are rather ideal for enhanced crystallization and monophasic product formation, the precise control of morphology and stoichiometry of the product in a hydrothermal process is quite complicated and tricky, down to the possibility of growth of secondary phases. In addition, very small changes in the hydrothermal parameters can lead to products with altogether different stoichiometry, and bulk as well as surface characteristics. Recently, considerable efforts have been made to formulate high surface area composites of MnO_2 with polymers [34], carbons [35,36], CNTs [32,36,37] and graphene [38] etc., to induce conductivity and achieve superior pseudocapacitance. However, composite materials are good to study under laboratory conditions, scaling up for practical applications need further evaluation. Further, composite materials may suffer from phase heterogeneity after initial charge-discharge cycles resulting in diminished pseudocapacitance performance. In addition, tuning the surface morphology, porosity as well as electrochemical properties of composite electrode materials is rather impractical. Hence enhancing the pseudocapacitance performance of single phase $\alpha\text{-MnO}_2$ by mesoscopic level modification of surface morphology and microstructures is quite essential. In this perspective,

nanostructurization, easily controllable pore and surface modification, and scalable fabrication of conductive nanoarchitectures, using simple, environmentally friendly and reproducible synthesis methods are the major challenges to produce suitably structured $\alpha\text{-MnO}_2$ for supercapacitor applications.

Lately, microwave-mediated synthesis, due to higher penetration depth, enhancement in the nucleation rate, lesser thermal gradient in the reaction medium and reduction in the synthesis time, has drawn great deal of attention in uniform nanostructurization of metal oxides [39]. In this context, microwave-mediated synthesis has been adopted to prepare MnO_2 with highly uniform microstructures [40–43]. However the microwave methods adopted in the literature to synthesize MnO_2 are few in number. In addition most of the microwave methods are exploited either under hydrothermal conditions [41–43] or in the presence of templates [40]. Since the hydrothermal reaction conditions as well as presence of organic surfactant molecules modify the kinetics and selectivity of crystal growth, the specific affect of microwave on the crystal growth and surface morphology of MnO_2 cannot be envisaged clearly. Further, there is hardly any literature available showing clear affect of microwave on the surface morphology and other physicochemical properties of $\alpha\text{-MnO}_2$. Therefore, it is important to distinguish the affect of microwave heating and the conventional heating, for the nature of crystal growth, surface morphology and structure–activity relationship of $\alpha\text{-MnO}_2$.

In this study, we have selectively synthesized hierarchically porous $\alpha\text{-MnO}_2$ in conventional-reflux and microwave mediated methods, under non-hydrothermal template-free synthesis conditions. Further, the physicochemical and structure-activity correlations have been studied in greater detail, to ascertain the rationale behind the suitability of microwave mediated synthesis over conventional-reflux synthesis of $\alpha\text{-MnO}_2$ for high performance supercapacitor application.

2. Experimental

2.1. Synthesis of $\alpha\text{-MnO}_2$ samples

Analytical grade KMnO_4 (SD Fine Chemicals, India) and HCl (Rankem, India) were used as received. Triply distilled water was used during all the experimental processes. In a typical batch of experiment, 22.2 mmol of HCl in 10 ml of water was added drop wise to 90 ml of 5.5 mmol aqueous KMnO_4 solution with constant stirring, to form the precursor solution. The precursor solution was then divided in to two equal halves, one half was subjected to refluxing at 120°C for 12 h, and the other half was subjected to microwave heating, using 250 W power at 120°C for 15 min, in a CEM Discover Bench Mate microwave reactor. The heat treatments resulted in the formation of black color compounds. After self-cooling the reaction mixtures to room temperature, the compounds were concentrated by centrifugation at 5000 rpm, with repeated washing in water to remove impurities and possible un-reacted starting materials. The materials were then dried overnight under vacuum, at 60°C , to get the final product. The samples synthesized under conventional-reflux and microwave assisted methods were assigned as $\text{MnO}_2\text{-ref}$ and $\text{MnO}_2\text{-mw}$, respectively.

2.2. Technical characterizations

Thermogravimetric analyses (TGA) of the samples were carried out on a TA-make Q500-V20.10 Build 36 TGA instrument in air flow (20 ml per min) with a linear heating rate of 20°C per min. The powder X-ray diffraction (PXRD) patterns were recorded from 10

to 80° at a scan rate of $0.01^\circ \text{ s}^{-1}$ using a Bruker AXS D8 Advance diffractometer, employing $\text{Cu-K}\alpha$ ($\lambda = 0.15408 \text{ nm}$) radiation generated at 40 kV and 30 mA. The crystallite size of the samples were estimated applying the Debye-Scherrer equation, $D = K\lambda/(\beta\cos\theta)$ where D is the linear dimension of the particle (particle size), K is the spherical shape factor (0.89) and β is the graphically measured full width at half maximum height (FWHM) of the particular peaks. Multipoint N_2 adsorption–desorption experiments were carried out at 77 K on an automatic Micromeritics ASAP 2020 analyzer. The samples are out-gassed at 100°C for 2 h followed by 150°C for 10 h in a dynamic vacuum before physisorption measurements. The specific surface areas were calculated by Brunauer–Emmett–Teller (BET) gas adsorption method and the pore size distribution plots were generated from desorption branch of the isotherm by the Barrett–Joyner–Halenda (BJH) method. The surface morphologies of the samples were obtained from an FEI Quanta FEG 200 field emission scanning electron microscope (FESEM). The powder samples were dispersed in ethanol by sonication and deposited on a conducting carbon tape before mounting on the microscope sample holder for analysis. The chemical compositions of the samples were analyzed using inductively coupled plasma–optical emission spectrometry (ICP-OES) in a Perkin Elmer Optima 5300 DV ICP-OES spectrometer.

2.3. Fabrication of electrode and electrochemical measurements

The working electrodes for evaluating the electrochemical properties were fabricated by mixing 80 wt% of each MnO_2 sample with 15 wt% of acetylene black in an agate mortar. To this mixture, 5 wt% polyvinylidene difluoride (PVdF) binder dissolved in 1-methyl-2-pyrrolidinone (NMP) was added to form slurry. The slurry was coated (area of coating : 1 cm^2) on a pre-treated battery-grade Ni foil (0.2 mm thick, polished with 991A softflex grade abrasive paper (Silicium Carbid P 2000) followed by sonication in ethanol for 1 h) and dried at 60°C for 8 h under vacuum. Cyclic voltammetry (CV), chronopotentiometry (CP) and electrochemical impedance spectroscopy (EIS) studies were performed using a CHI 7081C electrochemical workstation in a three-electrode configuration, with MnO_2 coated Ni plate, Pt foil ($1 \times 2 \text{ cm}^2$) and saturated calomel electrode (SCE) as working, counter and reference electrodes, respectively. All the electrochemical measurements were performed using 1.0 M aqueous Na_2SO_4 solution as the electrolyte. The electrochemical impedance spectra were measured by imposing a sinusoidal alternating voltage frequency of 10^{-2} to 10^5 Hz , alternating current (ac) amplitude of 5 mV and a constant dc bias potential of 0.5 V. All potentials reported in the present study are against SCE.

3. Results and discussion

3.1. Physicochemical characterizations

3.1.1. PXRD and TGA analyses

The PXRD patterns of MnO_2 -mw and MnO_2 -ref samples shown in Fig. 1A confirm the crystalline tetragonal α - MnO_2 phase (JCPDS: 44–0141) [22]. However, the crystallinity of α - MnO_2 samples synthesized from conventional-reflux and microwave mediated heating methods are drastically different as observed from the differences in intensity of PXRD patterns. The MnO_2 -mw sample shows intense and clear PXRD peaks exhibiting better crystallinity and phase purity as compared to MnO_2 -ref sample. This may happen due to hot spot induced rapid crystal growth during microwave mediated reaction. The higher thermal gradient in the conventional-reflux medium leads to α - MnO_2 with some non-stoichiometry and thus broader XRD peaks. The crystallite size of MnO_2 -mw and MnO_2 -ref samples calculated using Scherrer equation are $\sim 12 \text{ nm}$ and $\sim 9.5 \text{ nm}$, respectively. Structurally, α - MnO_2 possess 1D channel structure resulting from the double chains of interlinked MnO_6 octahedra (edge-shared). The MnO_6 octahedra are linked at the corners to form (2×2) and (1×1) tunnel structures extending in a direction parallel to the c axis of the tetragonal unit cell. The size of the (2×2) and (1×1) tunnels are ~ 0.46 and $\sim 0.189 \text{ nm}$, respectively [13,16,44]. Due to larger size, the (2×2) tunnels are suitable for possessing specific cations such as Na^+ , K^+ , NH_4^+ , Ba^{2+} , or H_3O^+ which stabilize the α - MnO_2 structure [45]. During our synthesis process, K^+ and H_3O^+ are the possible stabilizing cations, which may remain intercalated in the (2×2) tunnels of α - MnO_2 . Since the amount of K^+ ions in an α - MnO_2 lattice significantly influence many intrinsic properties [46,47], ICP-OES analyses have been performed to quantitatively find out the amount of K^+ in the MnO_2 -mw and MnO_2 -ref samples. The amount of K^+ ions in the MnO_2 -mw sample is found to be $\sim 10.2 \text{ wt\%}$, which is considerably higher than the K^+ ions present in MnO_2 -ref sample ($\sim 6.3 \text{ wt\%}$). Since the MnO_2 -mw sample possesses high crystal orderliness, the more number of K^+ ions are effectively involved in charge neutralization of the lattice.

For further structural insights, thermogravimetry analyses of the MnO_2 -mw and MnO_2 -ref samples have been performed and the respective TGA patterns are shown in Fig. 1B. Both the samples show progressive weight losses up to $\sim 500^\circ\text{C}$, which is ascribed to the removal of surface-adsorbed water. The TGA patterns of the samples also indicate that the removal of water molecules from α - MnO_2 lattice is a complex process which may proceed in two steps: (1) the removal of surface-adsorbed water molecules as well as uncoordinated interlayer water (up to $\sim 225^\circ\text{C}$) and (2) the water loss from the hydration shell of interlayer cations (up to $\sim 500^\circ\text{C}$)

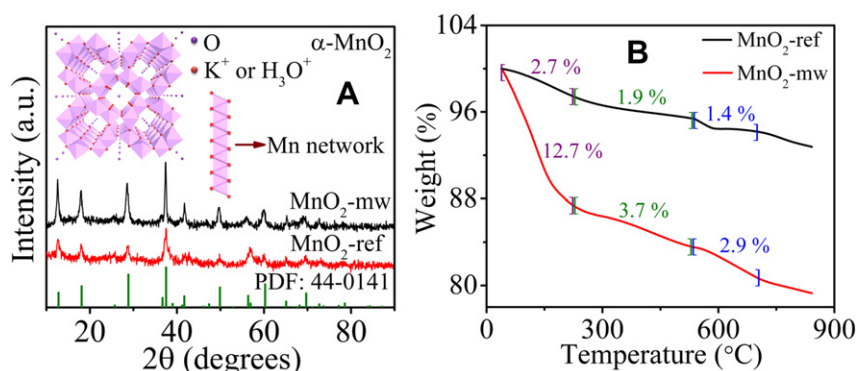


Fig. 1. (A) XRD patterns of MnO_2 -mw and MnO_2 -ref samples, and (B) their corresponding TGA profiles.

[48]. Quantitative estimations show $\sim 2.7\%$ and $\sim 12.7\%$ weight loss due to adsorbed-water from MnO_2 -ref and MnO_2 -mw samples, respectively. Similarly, hydrated-water losses from MnO_2 -ref and MnO_2 -mw samples are estimated as $\sim 1.9\%$ and $\sim 3.7\%$, respectively. The higher loss of adsorbed as well as coordinated water from the MnO_2 -mw can be attributed to higher porosity and accessible surface area of the sample. Further, the presence of higher amount of cation coordinated water in the MnO_2 -mw sample correlates well with higher amount of K^+ from ICP-OES analysis. Additional weight loss of $\sim 1.4\%$ for MnO_2 -ref and $\sim 2.9\%$ for MnO_2 -mw sample at $\sim 535^\circ\text{C}$ corresponds to the transformation of MnO_2 to Mn_2O_3 ($4\text{MnO}_2 \rightarrow 2\text{Mn}_2\text{O}_3 + \text{O}_2$) [48]. The nature of weight loss is noticeably sharper in the case of MnO_2 -ref sample as compared to the MnO_2 -mw sample. This is due to the presence of lesser amount of K^+ ions in the (2×2) tunnel of MnO_2 -ref lattice which provides poor stabilization to the crystal structure as compared to MnO_2 -mw lattice. Due to the hindrance of K^+ ions during the phase transition in MnO_2 -mw lattice, the characteristics weight loss after $\sim 535^\circ\text{C}$ is quite sluggish. The weight losses after $\sim 700^\circ\text{C}$ in both the samples correspond to the phase transition of Mn_2O_3 to Mn_3O_4 ($3\text{Mn}_2\text{O}_3 \rightarrow 2\text{Mn}_3\text{O}_4 + 1/2\text{O}_2$) [48].

3.1.2. FESEM analysis

FESEM analyses have been performed to probe the surface structural identities of MnO_2 -mw and MnO_2 -ref samples and the respective microscopic images are shown in Fig. 2 (A, B) and (C, D). The MnO_2 -ref sample (Fig. 2A and B) shows congregation of distorted and irregular flower like structures made up of thick microsheets, whereas MnO_2 -mw sample (Fig. 2C and D) shows

highly uniform and porous flower like structure made up of thin layered microsheets. The observed difference in the dimensionality and arrangement of the microsheets resulting in the characteristic morphology of the MnO_2 -ref and MnO_2 -mw samples is solely due to the difference in the mode of heating during synthesis [49]. The exact mechanisms for the formation of this type of complex superstructures are yet to be understood clearly, due to wide range of interactions such as van der Waals, ionic, steric, entropic and electrostatic, occurring simultaneously in the reaction medium with varying strength, range, and selectivity [50]. However, time dependent product analysis during synthesis as well as some theoretical studies show that the generation of these types of irregular as well as highly ordered surface structures is mostly due to the self-assembly process during structural growth [51]. By and large, the formation of the hierarchical structures follows a nucleation-dissolution-anisotropic growth-recrystallization mechanism [52]. Further, the self-assembly process can be enormously affected by the mode of heat treatment during synthesis. In both the conventional-reflux and microwave-mediated methods, the K^+ ion induces formation of MnO_2 microflakes during the initial nucleation process [47]. With further course of reaction at elevated temperature, the metastable micro-flakes tend to curl resulting in twisted microflakes [46]. Under conventional-reflux heating conditions for longer duration, the curled microflakes undergo coalescence and Ostwald ripening to form thick microflakes. As the reaction proceeds further, the microflakes undergo random self-assembly to generate distorted and irregular flower like structure. However, during the microwave-mediated synthesis, the nature and distribution of bulk temperature in the reaction medium is

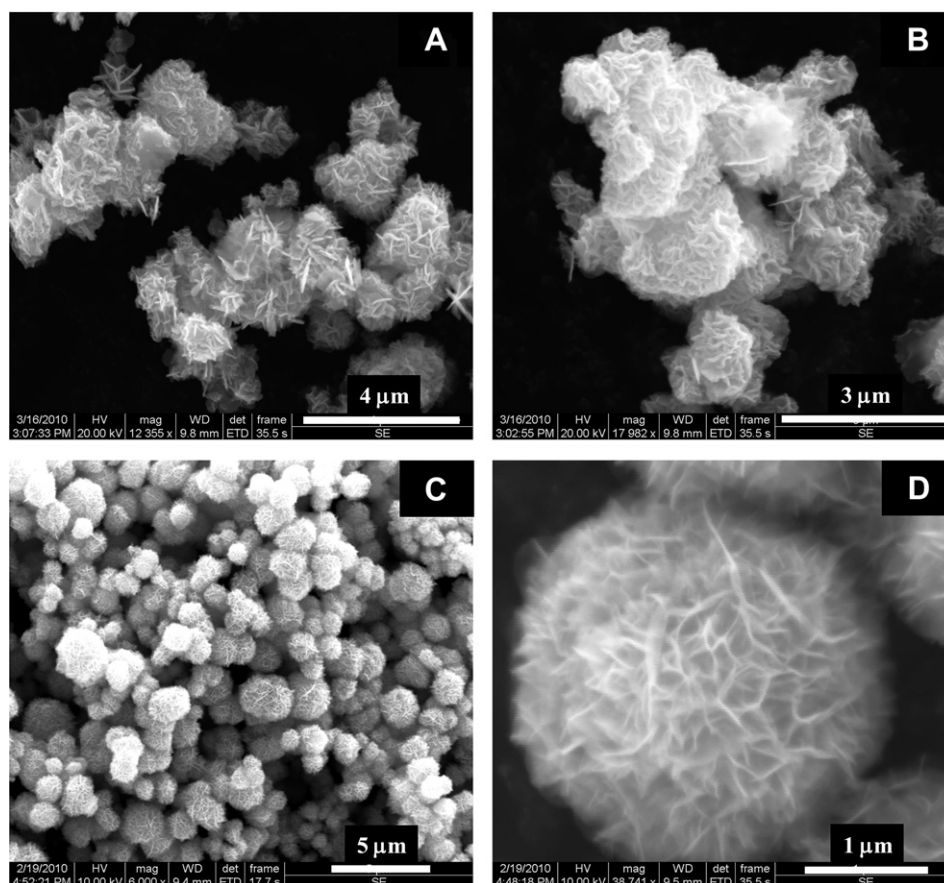


Fig. 2. FESEM micrographs of MnO_2 -ref (A and B) and MnO_2 -mw (C and D) samples.

entirely different due to unique microwave dielectric heating mechanism, which occurs through dipolar polarization and more importantly ionic conduction [39,49]. In fact, microwave not only accelerates the nucleation but also enhances the rate of dissolution of precursor, the formation of intermediate polynuclear species as well as amorphous intermediary particles, and agglomeration of primary particles. Microwave also creates hot spot on the precursors and greatly affects the mode and rate of self assembly/aggregation. The localized heating by microwave also induces the superior crystallization of the product [39,49]. This phenomenon is reflected in the PXRD pattern, where $\text{MnO}_2\text{-mw}$ sample is found to be more crystalline as compared to $\text{MnO}_2\text{-ref}$ sample. Further, microwave also randomly etches the partially coalesced flakes to provide a type of rippled surface to the flakes [49]. The curled and rippled flakes then undergo uniform and directional self-assembly by mass transport mechanism induced by microwave created localized “hot surface” [39,49]. The self assembly results in well arranged ball like superstructure with hierarchical rippled shaped surface. It should be noted that, the absence of such unique heating mechanism in the conventional-reflux method leads to product with no specific morphological arrangement. The plausible formation mechanisms of $\text{MnO}_2\text{-ref}$ and $\text{MnO}_2\text{-mw}$ samples are presented in Scheme 1, which is consistent with the well studied formation mechanisms of metal oxides from time-dependent product analysis [53].

3.1.3. BET analysis

The hierarchical porosity of $\text{MnO}_2\text{-ref}$ and $\text{MnO}_2\text{-mw}$ samples are probed from the BET analysis. Fig. 3 shows the N_2 -adsorption/desorption isotherms of $\text{MnO}_2\text{-ref}$ and $\text{MnO}_2\text{-mw}$ samples, and the inset shows the corresponding BJH pore size distribution plots. The isotherms of both the samples show H3-type hysteresis loops which mostly correspond to the presence of aggregated plate like particles with slit shape pores [54]. The average pore diameters of $\text{MnO}_2\text{-ref}$ and $\text{MnO}_2\text{-mw}$ samples are found to be in the mesopore region, with bimodal pore size distributions. However, the pore size distribution maxima of the samples are centered at different pore radii; for $\text{MnO}_2\text{-ref}$ sample, the maxima are centered at ~ 5.7 and ~ 10.3 nm, whereas those in $\text{MnO}_2\text{-mw}$ sample at ~ 3.9 and ~ 12.7 nm. These results show that mesopores of different sizes originate from the difference in the surface structures of $\text{MnO}_2\text{-ref}$ and $\text{MnO}_2\text{-mw}$ samples. The intensities of the pore size distribution in $\text{MnO}_2\text{-mw}$ sample are substantially higher than that of $\text{MnO}_2\text{-ref}$ sample suggesting higher pore volume of $\text{MnO}_2\text{-mw}$ sample. The characteristic bimodal porosity of the samples is an amalgamation of internal space of the agglomerated flakes, surface porosity of the flakes, and the porosity due to internal space of different mesoflower structures [55]. The pore size distribution of $\text{MnO}_2\text{-mw}$ sample is rather narrow as compared to $\text{MnO}_2\text{-ref}$ sample which

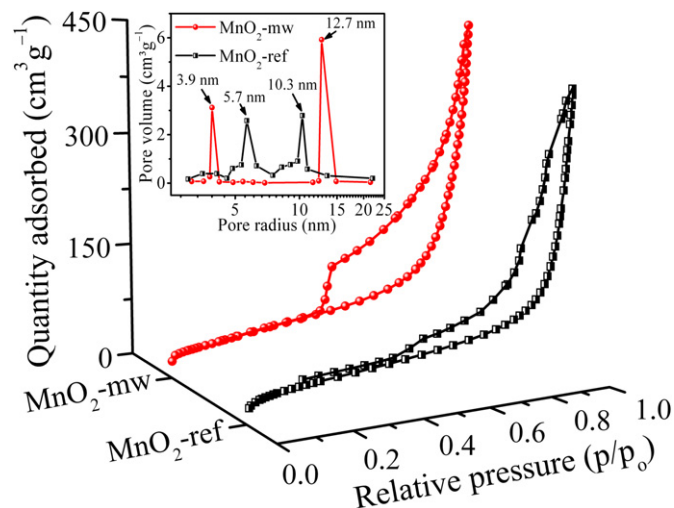


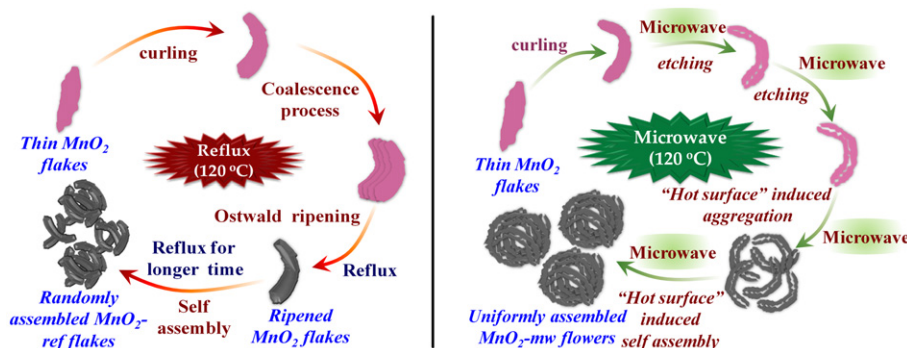
Fig. 3. N_2 -adsorption–desorption isotherm plots of $\text{MnO}_2\text{-ref}$ and $\text{MnO}_2\text{-mw}$ samples. Inset shows the corresponding pore size distribution graphs of the samples.

further supports the better homogeneity in the surface morphology and porosity of $\text{MnO}_2\text{-mw}$ sample. The BET surface area and corresponding pore volumes of $\text{MnO}_2\text{-mw}$ and $\text{MnO}_2\text{-ref}$ samples are 155 and $130 \text{ m}^2 \text{ g}^{-1}$, and 0.67 and $0.56 \text{ cm}^3 \text{ g}^{-1}$, respectively. Such type of hierarchical surface morphologies with well developed pore structures are advantageous for energy storage applications since large pore channels permit rapid electrolyte transport, while the small pores provide more active sites for chemical reactions [5].

3.2. Electrochemical characterizations

3.2.1. Cyclic voltammetry (CV) analysis

To explore the potential applications in electrochemical energy storage, the hierarchical porous MnO_2 samples were used to make supercapacitor electrodes, and characterized with cyclic voltammetry, galvanostatic charge/discharge and impedance measurements [56]. The CV responses of the $\text{MnO}_2\text{-ref}$ and $\text{MnO}_2\text{-mw}$ samples carried out at different scan rates ($10\text{--}100 \text{ mVs}^{-1}$) in a fixed potential range of 0–1.0 V in aqueous 1 M Na_2SO_4 electrolyte are shown in Fig. 4A and B, respectively. The individual $\text{MnO}_2\text{-ref}$ and $\text{MnO}_2\text{-mw}$ sample electrodes were subjected to one time stabilization/activation by repeated CV cycles (50 numbers) at sweep rates of 5 mVs^{-1} in the similar potential range, before performing the CV experiments for accessing the electrochemical performance. The CV profiles of MnO_2 samples at different scan rates are almost rectangular in shape indicative of ideal



Scheme 1. Probable mechanisms for the formations of (A) $\text{MnO}_2\text{-ref}$ and (B) $\text{MnO}_2\text{-mw}$ samples.

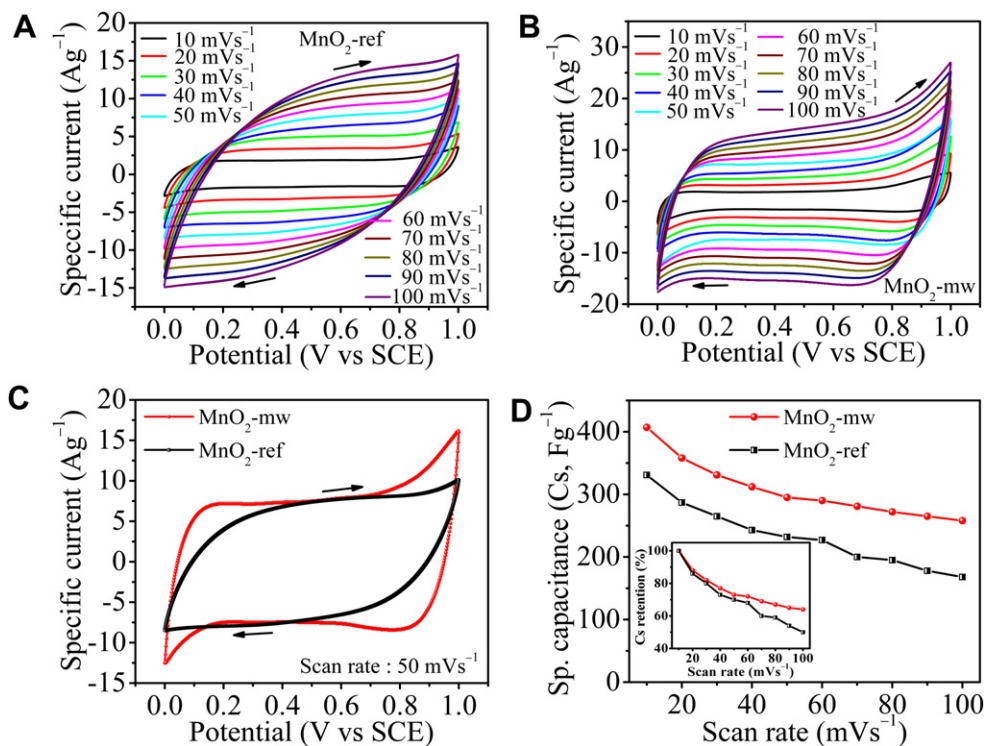
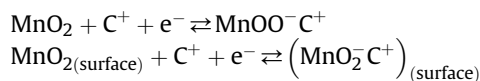


Fig. 4. Cyclic voltammograms of (A) MnO₂-ref and (B) MnO₂-mw samples at different scan rates; (C) Comparison of cyclic voltammograms of MnO₂-ref and MnO₂-mw samples at 50 mVs⁻¹ and; (D) Specific capacitance versus scan rate plots of MnO₂-ref and MnO₂-mw samples; inset shows the plots of capacitance retention with potential scan rate.

pseudocapacitive behavior [2,5,14]. The redox chemistry of MnO₂ during cyclic voltammetry study is largely dependent on the nature of the electrolyte, i.e. acidic, basic or neutral [57]. In neutral electrolyte as studied here, there are generally two parallel mechanisms proposed, based on the adsorption and intercalation involving surface and bulk phenomena during the charge storage in porous MnO₂-based electrodes [18,19,45,58]. The first possible mechanism is the intercalation and de-intercalation of smaller H⁺ or bigger alkali metal cations such as Na⁺ in the matrix of the material during the reduction and oxidation process, respectively [19,58]. The other possible mechanism is based on the adsorption of the H⁺ and Na⁺ ions on the surface, rather than in the bulk of the sample [19,58]. The primary reactions involved in the two possible processes can be represented as:



where, C can be either H⁺ or Na⁺ ion. From the CV graphs it is realized that there is an increase in the anodic (positive) and cathodic (negative) current density with increase in the scan rate, during CV cycling. This clearly demonstrates the occurrence of intercalation and de-intercalation of H⁺ or Na⁺ ions during the charge storage in the MnO₂ samples. This is due to the fact that at lower scan rates, both outer- and the inner-pore surfaces of the porous electrode materials are effectively utilized for intercalation, while at high scan rates mainly outer regions of the pores are accessed by the ions [59,60]. However, at a fixed potential scan rate, the measured specific current of MnO₂-mw sample is marginally higher than that of MnO₂-ref sample (Fig. 4C). It is known that the characteristics of redox reactions are strongly dependent on the shape and dimensionality of the electrode material at the nanoscale level [10,14,61–63]. Two main factors; (1) higher specific area and (2) suitable porosity for easy insertion/de-insertion of ions into/

from the electrode matrix mostly contribute to the number, efficiency and ease of redox reactions. The MnO₂-mw sample consists of numerous rippled shaped microflakes with higher porosity as compared to the lowly porous MnO₂-ref sample made up of thick microflakes. It is therefore presumed that the morphologically preferable MnO₂-mw sample contains more surface than bulk which promotes higher number of redox reactions resulting in higher current density as compared to that of MnO₂-ref sample. Further the characteristic cyclic voltammetry patterns of MnO₂-mw sample are better rectangular as compared to MnO₂-ref sample even at higher scan rates, which is solely due to less polarization resistance (better accessibility of the surface to ions) in the MnO₂-mw sample [20]. The structural suitability of MnO₂-mw sample facilitates faster ion diffusion between the electrode matrix and the electrolytes, thereby reducing the polarization resistance even at higher scan rate conditions. From the CV measurements at different scan rates (ν , Vs⁻¹), the specific capacitance (Cs, Fg⁻¹) values are estimated using the equation [2,64–66]:

$$Cs = \frac{1}{\nu w (V_a - V_c)} \int_{V_a}^{V_c} i \times V dV \quad (1)$$

where w (g) is active weight of the electrode material. The specific capacitance values of the samples at different scan rates were drawn from the integration of potential (V versus SCE) versus specific capacitance (Cs, Fg⁻¹) graphs, as shown in Fig. S1 in the Supplementary Information. At potential scan rates of 10–100 mVs⁻¹, the specific capacitance values for MnO₂-mw sample are found to be 407–258 Fg⁻¹. Similarly, at the same scan rates the specific capacitance values for MnO₂-ref sample are in the range of 331–168 Fg⁻¹. The CV data show that there is a continuous decrease in the specific capacitance values with increase in potential scan rate (Fig. 4D). This is an important aspect of porous

materials where the resistance of the pores plays a significant role during charge storage process [59,60]. At lower potential sweep rate, the output current is small, so IR loss (voltage drop) is negligible, and the overall current response is mostly capacitive. However, with increase in scan rate, the current becomes more and the IR loss gradually becomes significant, which results in decrease in the reduced current and the response current become more resistive. Therefore, the specific capacitance becomes inversely correlated with the scan rate [59,60]. Nevertheless, the pore structure of an electrode material can influence the distributed resistance inside the pores which further controls the nature of response current (capacitive or resistive) during CV cycling. An electrode material with suitable pore structure (easy channeling of ions) contributes positively toward the capacitive nature of response current and charge storage efficiency [67]. As in the MnO₂-mw sample the pores are more regular, the ionic mobility is less hindered, which minimize resistance inside the pores. This is reflected in the higher specific capacitance value and only ~36% capacitance loss with increase in the scan rate from 10 to 100 mVs⁻¹. However, during similar CV scans, MnO₂-ref sample shows lower specific capacitance value and suffers ~50% capacitance loss with increase in the scan rate from 10 to 100 mVs⁻¹ (inset of Fig. 4D). This demonstrates the higher current response of MnO₂-mw sample, which is due to the high accessibility of H⁺ and Na⁺ ions on the surface consisting of numerous nano-channels. The specific capacitance values of the MnO₂-mw sample is also reasonably higher than the values reported for non-composite MnO₂ materials in the given potential range, under higher loading conditions (~1 mgcm⁻²) and high scan rates. This may be due to the crystallographic phase purity, highly accessible active surface and surface homogeneity of the MnO₂-mw sample which possesses higher concentration of active adsorption sites (surface hydroxyl groups) thereby adding some non-Faradaic contribution

toward the charge storage [20]. It is to be noted from the inset of Fig. 4D that the % decrease in specific capacitance of MnO₂-ref and MnO₂-mw samples at lower scan rate are not so significant. This is due to the bulk accession/total surface accession by H⁺ and Na⁺ ions at lower scan rates. However at higher scan rates, the dominance of only surface accession phenomena results in the larger variation in the decrease of specific capacitance values.

3.2.2. Chronopotentiometry (CP) analysis

Owing to the importance of cyclic stability during charge-discharge of electrode materials for their potential use in super-capacitor devices, linear voltage–time profiles of the MnO₂-ref and MnO₂-mw samples measured at current densities of 1, 2, 4, 8 and 16 Ag⁻¹ are shown in Fig. S2A and B, respectively, in the Supplementary Information. The rate dependent discharge profiles taken from the first cycles of corresponding voltage–time profiles of MnO₂-ref and MnO₂-mw samples are shown in Fig. 5A and B, respectively. It is to be noted that the discharging time of MnO₂-mw sample is higher than that of MnO₂-ref sample at identical current density conditions. A comparative discharge profile of MnO₂-ref and MnO₂-mw samples at 8 Ag⁻¹ is shown in Fig. 5C. This in principle represents enhanced pseudocapacitance performance of the MnO₂-mw sample. In addition, the galvanostatic charge/discharge profiles of the MnO₂-mw sample (Fig. S2B) are more linear and symmetrical as compared to the MnO₂-ref sample (Fig. S2A), which indicates better I–V response, electrochemical reversibility and ideal capacitive characteristic of the microwave synthesized sample [2]. Specific capacitance values of MnO₂-ref and MnO₂-mw samples have been calculated from the linear voltage–time measurements at different applied current densities (i), active mass of the sample (m), corresponding discharge time (Δt) and operating potential window (ΔV) using the equation [2,64–66]:

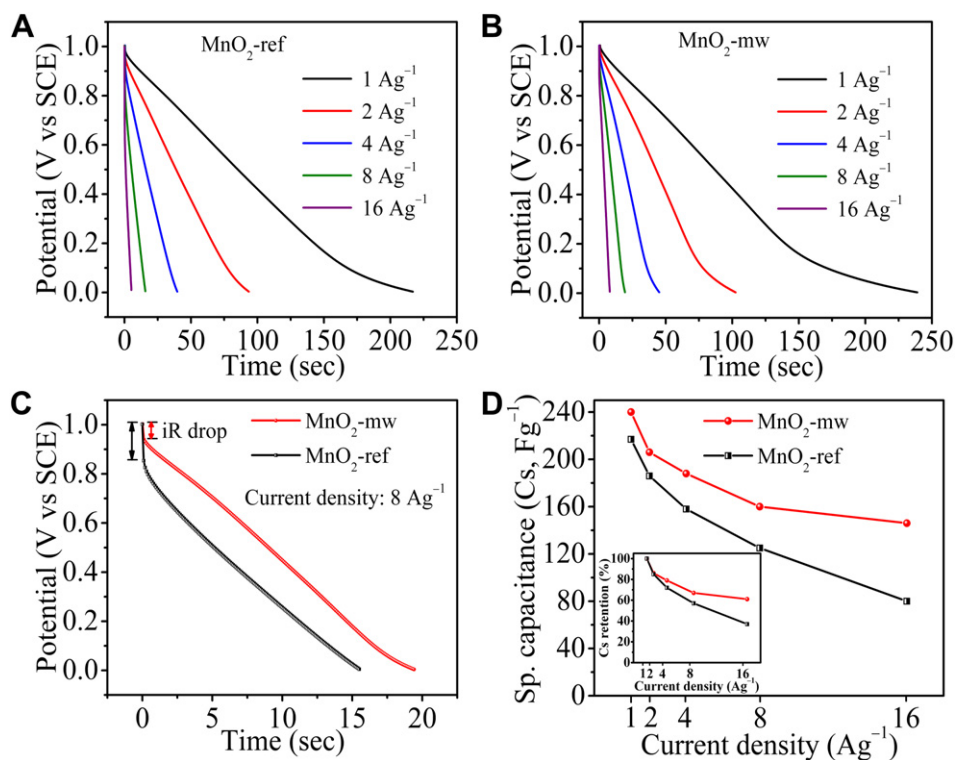


Fig. 5. Discharge curves of (A) MnO₂-ref and (B) MnO₂-mw samples at different current densities; (C) Comparison of iR drops in the discharge profiles of the samples at current density of 8 Ag⁻¹; and (D) Current density dependent specific capacitance plots of the samples; inset shows the plots of capacitance retention versus applied current density.

$$Cs = \frac{i}{m(\Delta V/\Delta t)} \quad (2)$$

The estimated specific capacitance values of MnO₂-mw and MnO₂-ref sample at different applied current densities of 1.0–16.0 Ag^{−1} are presented in Fig. 5D. From the current density versus capacitance retention plots of the samples in the inset of Fig. 5D, it can be ascertained that the MnO₂-mw sample retains ~61% of specific capacitance as compared to ~36% specific capacitance retention by MnO₂-ref sample at 16 Ag^{−1} against the corresponding values at current density of 1 Ag^{−1}. These performance data suggest excellent higher rate electrochemical performance of hierarchically porous MnO₂-mw sample as compared to MnO₂-ref sample [2,55,62,63]. The good capacitive retention behavior of MnO₂-mw sample is a combined contribution of high porosity with superior pore-channel structure and large internal accessible surface which in turn facilitate the electrolyte penetration into the sample matrix, decrease the ion diffusion resistance and enhance the electro-active surface utilization during the redox process [17,68,69]. Besides, the nanosize channels in the rippled shape surface of MnO₂-mw sample alleviate ion hopping between the neighboring surface sites, thereby easing the ion diffusion and increasing the dynamics of charge propagation during the charge storage process [49,70]. Further, numerous nanochannels and higher pore volume of the sample act as “ion-buffering reservoirs” which reduce the mean free path of the anions and facilitate faster ionic and electronic kinetics, thus maximising the reversible insertion/de-insertion reactions [49,55,65,71]. The MnO₂-ref sample, due to lower surface area, pore volume and agglomerated thick flake like structure, contains lower number of electro-active surface sites, and the irregular pores as well as disoriented pore walls induce random scattering of H⁺ and Na⁺ ions, which enhance the diffusion resistance and decrease the kinetics of these ions inside the sample matrix [69]. Therefore the overall ion transport resistance is less in MnO₂-mw sample as compared to MnO₂-ref sample. The higher resistance in the MnO₂-mw sample can also be established from the lower voltage (iR) drops during the discharge process at all current densities [72,73] as shown in Fig. S2A and B and the compared iR drops at 8 Ag^{−1} in Fig. 5C. The superior bulk accessibility in MnO₂-mw sample as compared to MnO₂-ref sample by H⁺ and Na⁺ ions is presented in Scheme 2.

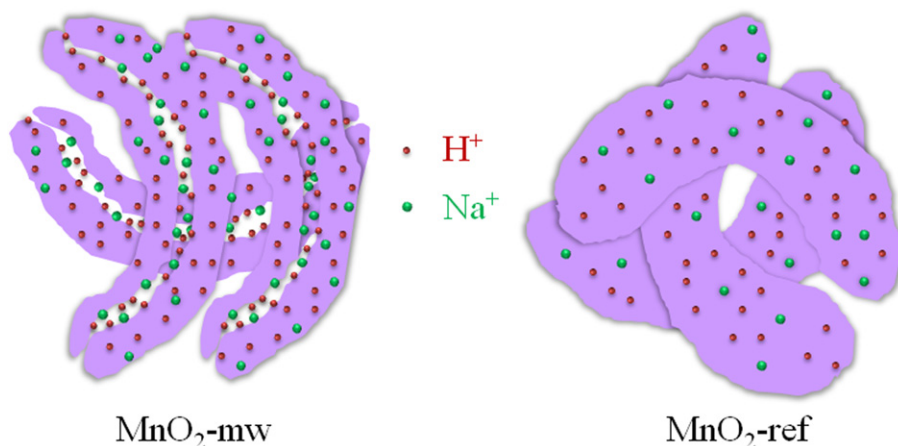
Long cyclic stability is one of the most important requirements for practical competence of supercapacitor devices. The cyclic specific capacitance performance of MnO₂-ref and MnO₂-mw

samples for 400 cycles at each current density of 1.0, 2.0, 4.0, 8.0 and 16.0 Ag^{−1} are presented in Fig. 6A and B, respectively, with corresponding capacitance retention plots shown in Fig. 6C and D. From these data plots, it is quite evident that the decrease in specific capacitance with increasing applied current densities is considerably higher for MnO₂-ref sample as compared to MnO₂-mw sample. The superior capacitance retention of MnO₂-mw sample is attributed to the microwave induced oriented three dimensional network structures which do not suffer pore and surface structural degradation during repeated charge-discharge process even at higher current density conditions. The easy channeling of H⁺ and Na⁺ ions exert minimum strain and deformity on porous MnO₂-mw sample during continuous insertion/de-insertion process. In contrast, the thick microflakes of MnO₂-ref sample are very loosely assembled and there is no regular and three-dimensional nanoporous architecture to compensate the strain exerted by fast insertion/de-insertion of H⁺ and Na⁺ ions. Therefore MnO₂-ref sample suffers structural deformation and flaking-off, particularly under high current density condition for long cycles, resulting in poor capacitance retention. For both the samples, there is minor increase in the specific capacitance during the first 100 to 150 charge–discharge cycles at lower current density conditions. This is due to surface activation and minor pore opening during the bulk participation in ion insertion/de-insertion, particularly at lower current density conditions.

The Coulombic efficiency (η) of the charge storage process is an assessment of easiness at which ion insertion and de-insertion takes place during charging and corresponding discharging processes, respectively [49,55,65]. The Coulombic efficiency (%) of the samples has been quantitatively estimated using the following equation:

$$\eta = \frac{t_D}{t_C} \times 100 \quad (3)$$

Where t_C and t_D represents charging and discharging time, respectively (Fig. S2A and B, in the Supplementary Information). From the compared Coulombic efficiency patterns of MnO₂-ref and MnO₂-mw samples during long charge–discharge cycles at different current densities in Fig. S3A and B, it can be seen that the performance of MnO₂-mw sample is significantly better than that of MnO₂-ref sample. The surprising increase in the Coulombic efficiency with increase in applied current density during the charge-discharge measurements on MnO₂-mw sample is due to faster surface activation at high current density condition. The



Scheme 2. The accessibility of H⁺ and Na⁺ ions inside the matrix of MnO₂-mw and MnO₂-ref samples. The nanochannels of the MnO₂-mw sample matrix facilitate more ion diffusion inside the bulk.

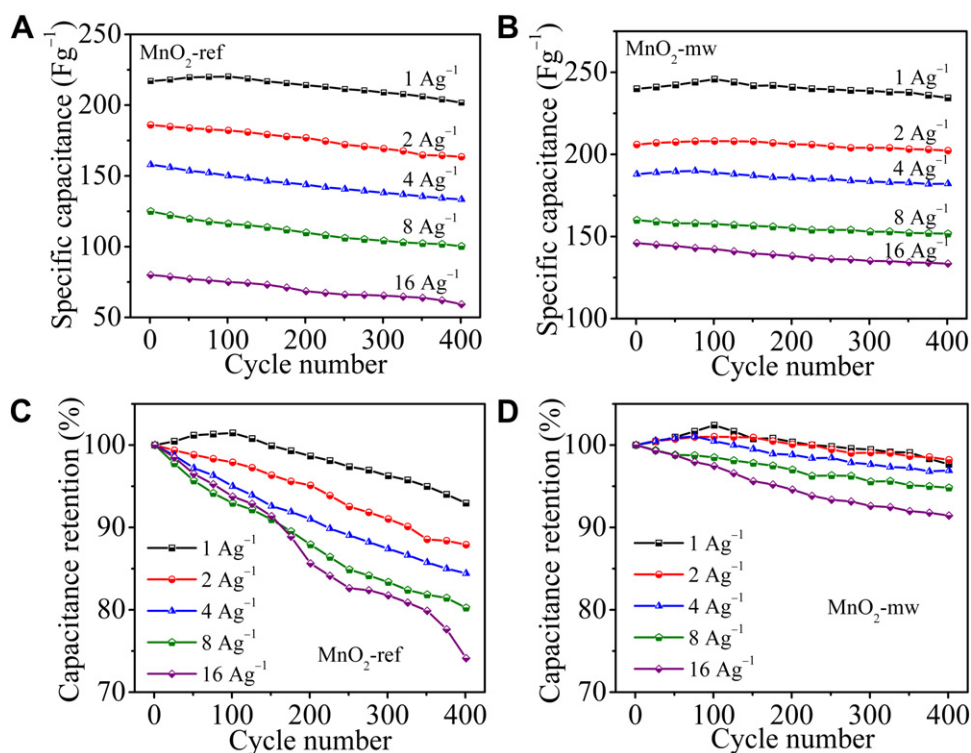


Fig. 6. Specific capacitance and % capacitance retention of MnO_2 -ref (A and C) and MnO_2 -mw (B and D) samples with cycle number, derived from the chronopotentiometry study.

~100% Coulombic efficiency of MnO_2 -mw sample at higher current density conditions signifies lower internal resistance, shorter ion transport distances and better electro-active surface utilization due to insignificant structural deformation and phase transformation [49,55,65] even after long charge-discharge cycles. All these results clearly demonstrate that microwave synthesized α - MnO_2 is a better electrode material over reflux-synthesized α - MnO_2 for super-capacitor device applications.

3.2.3. Electrochemical impedance spectroscopy (EIS) analysis

The EIS has been employed to study the kinetic features of MnO_2 -ref and MnO_2 -mw sample electrodes during their charge storage process [74]. For both the samples, the complex-plane impedance plots (Nyquist plots; imaginary part, Z'' versus real part, Z') fitted by complex nonlinear least squares (CNLS) fitting method to the Randle equivalent circuit are shown in Fig. 7A. The Nyquist plots of both the samples show almost similar profiles with two semicircles at higher frequency region followed by a spike at lower frequency region. The slopes of the spikes are close to 90° along the imaginary axis (Z'') which is a characteristic of non-ideally polarizable electrode, attributable to the occurrence of pseudocapacitance phenomena in the system [74]. Due to three characteristic impedance plot patterns at different frequencies, three major possible electrochemical processes are assumed in the electrode–electrolyte interface at high, medium, and low frequency regions. The nature of different kinetic processes in MnO_2 -ref and MnO_2 -mw samples at different frequency regions are assumed due to possible dissimilarity in the charge propagation phenomena on typical surface structures of the samples. At high frequency region, the small semicircle signifies charge transfer process in the electrode–electrolyte interfaces [60,75]. This can be suitably modeled as a double-layer capacitor, C_d (537.8 and $593.4 \mu\text{F cm}^{-2}$ for MnO_2 -ref and MnO_2 -mw samples, respectively) in parallel with a charge-transfer resistor, R_{ict} . The charge transfer

resistance at the electrode–electrolyte interface arises due to the discontinuity in the charge transfer process because of conductivity difference between the solid oxide (electronic conductivity) and liquid electrolyte phase (ionic conductivity) [60,75]. At the high frequency region, the intercept of the semicircles at real part ($Z' = 4.5 \Omega$) signifies a combination of ionic resistance of electrolyte, intrinsic resistance of substrate, and contact resistance at the active material/current collector interface. From the Nyquist plots in Fig. 7A, the cumulative resistances at higher frequency region are same for both the MnO_2 samples, suggesting combined contributions from ionic resistance of electrolyte, intrinsic resistance of substrate, and contact resistance at the active material/current collector interface. The resistance in medium frequency region is a result of diffusion controlled process, and the overall intrinsic capacitance and resistance are characteristic of ion insertion/de-insertion processes. These specific phenomena can be represented as a combination of film capacitor (C_f) in parallel with an electron-transfer resistor (R_{ect}). The distinctive semicircles of the MnO_2 -mw sample in the medium frequency region is small as compared to that for the MnO_2 -ref sample suggesting lower diffusion resistance during insertion/de-insertion of H^+ and Na^+ ions inside the matrix of porous MnO_2 -mw sample. This is consistent with the observations from CV and charge-discharge measurements. The presence of buffering H^+ and Na^+ ions inside the well-organized mesoporous matrix of MnO_2 -mw reduces the transport length of the ions inside the nanochannels, and hence the diffusion resistance. In contrast, the MnO_2 -ref sample lacks suitable regular porosity due to the absence of nanochannels, and suffers from higher ion diffusion resistance. The slope of 45° portion (shown as θ in Fig. 7A) in the transitory frequency next to the second semicircle and the noticeable linear part at the low frequency region of the respective Nyquist plots is called Warburg resistance (W) which originates from the frequency dependence of ion diffusion/transport from the electrolyte to the electrode surface

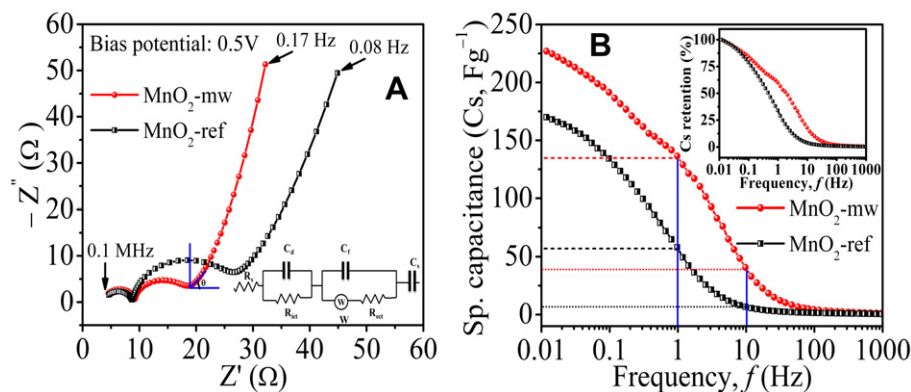


Fig. 7. (A) Complex plane impedance plots (Nyquist plots) of MnO₂-ref and MnO₂-mw samples; inset shows the Randles equivalent circuit from which the plots are generated; (B) Frequency dependent specific capacitance of MnO₂-ref and MnO₂-mw samples; inset shows the frequency dependent capacitance retention (%) of the samples.

[60,75]. The linear part which is almost vertical to the real axis in the imaginary part of the impedance at the low frequency region represents the Faradic pseudo-capacitance of the sample electrode. The equivalent series resistance (ESR), which is a measure of conductivity of an electrode material, has been obtained from the tangential intersection of the corresponding Nyquist plots on Z' -axis [76]. The ESR values of the MnO₂-mw and MnO₂-ref samples are found to be $\sim 15.9 \Omega$ and 21.3Ω , respectively, clearly suggesting higher conductivity of MnO₂-mw sample. The XRD results indicate that, MnO₂-mw sample is more crystalline and can have better defined tunnel/interlayer structure than MnO₂-ref sample. These characteristic physicochemical properties of MnO₂-mw sample favor better accommodation and transportation of cations. Easy conduction/transportation of cations throughout the bulk of MnO₂ is essential for enhanced pseudocapacitance performance. In this context, hydrated contents are also known to have positive influence on the ionic conductivities, since higher water content promotes proton hopping throughout the sample matrix [15]. From the TG analysis it is found that the MnO₂-mw sample contains significantly higher amount of water molecules than the MnO₂-ref sample. The presence of higher amount of water molecules can further enhance the proton conductivity in the sample matrix, thereby increasing the conductivity of MnO₂-mw sample. Therefore, the crystallographic identity of the electrode material is as important as active surface area for charge storage efficiency. The specific capacitance (C_s) values of both the MnO₂ sample electrodes have been derived from the impedance data, using frequency (f) and the imaginary Z'' ($=|-Z''|$) in the equation [64,65,74]:

$$C_s = \frac{1}{2\pi f Z''} \quad (4)$$

The frequency dependent specific capacitance plots of MnO₂-mw and MnO₂-ref samples are shown in Fig. 7B. From the plot, the specific capacitance values of MnO₂-mw sample are found to be considerably higher than MnO₂-ref sample, in the entire operating frequency range. Further, the specific capacitance values of MnO₂-mw sample are higher at elevated operating frequencies (135 Fg^{-1} at 1 Hz and 37 Fg^{-1} at 10 Hz) compared to MnO₂-ref sample (59 Fg^{-1} at 1 Hz and only 7 Fg^{-1} at 10 Hz), demonstrating higher frequency response of MnO₂-mw sample. It is known that the variation of capacitance with frequency is a common phenomenon for a porous electrode, which can be analyzed by the transmission line model first proposed by de Levie [77]. This model suggests that in the case of sufficiently high ac frequency, only the outer surface (near pore opening) is influenced by the ac voltage due to the smaller penetration depth

of the pore as compared to the pore length of the porous electrodes [77]. Therefore, the resultant capacitance is small since only a limited part of electrode surface is utilized as a capacitor. However, in the low frequency region, the penetration depth becomes larger as compared to the pore length, which results in more resultant capacitance due to maximum pore surface utilization. Hence, the superior capacitance response at higher frequency essentially suggests better bulk utilization of the electroactive sample, i.e. MnO₂-mw sample in the present study. According to the fractal tree-root model, the mesopores are more quickly charged as compared to the micropores due to the ease of mass transfer in the mesopores during the charge-discharge process [74]. Since, MnO₂-mw sample possess higher fraction of accessible three dimensional networks of regular mesopores, it shows better frequency response. However, due to the lower fractions of mesopores in MnO₂-ref sample, the charge transfer resistance becomes dominant as a result of severely random ionic collisions. The situation becomes worse at higher operating frequency and therefore the capacitor frequency response is low for MnO₂-ref sample. This is clearer from the frequency dependent capacitance retention (%) plot in the inset of Fig. 7B, where the MnO₂-mw sample shows higher capacitance retention than the MnO₂-ref sample at higher operating frequency condition. The better rate response and power performance of MnO₂-mw sample has been further verified from the capacitor response frequency [74]; the frequency where the phase angle $\varphi = -45^\circ$, ($f_\varphi = -45^\circ$), in the f versus φ plot in Fig. 8. The capacitor response frequency (0.364 Hz) of MnO₂-mw sample is appreciably higher than the response frequency (0.097 Hz) of MnO₂-ref sample. Since response time of a supercapacitor is the reciprocal of the response frequency, MnO₂-mw sample would show faster response (smaller response time) as compared to MnO₂-ref sample (larger response time) when used in a device.

Power density (d_p) and energy density (d_E) are most important parameters of electrochemical supercapacitor device which determine its operational performance/efficiency. The d_E values of MnO₂-ref and MnO₂-mw samples are derived from the CV measurements at different scan rates from the equation [78]:

$$d_E = \frac{1}{2} C V^2 \quad (5)$$

where C is the specific capacitance (Fg^{-1}) at a particular potential scan rate under the potential window of 1.0 V (Fig. 4A and B). The d_p values of the samples are derived by dividing the respective d_E values with time " t " for one cyclic sweep at the corresponding scan rate:

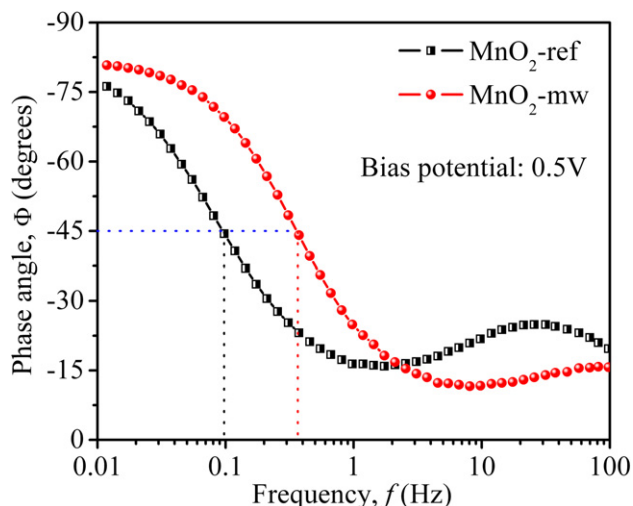


Fig. 8. The frequency dependence of phase angle, ϕ , for MnO_2 -ref and MnO_2 -mw samples.

$$d_p = \frac{d_E}{t} \quad (6)$$

The d_p versus d_E for the MnO_2 -ref and MnO_2 -mw samples are plotted and compared with the standard Ragone plot [79] for fuel cells, conventional batteries, conventional capacitors, and normal ultracapacitors in Fig. 9. Both MnO_2 -ref and MnO_2 -mw sample electrodes demonstrate relatively higher energy density than conventional capacitors and normal ultracapacitors, maintaining their power density considerably higher than the conventional batteries and fuel cells. This observation is quite promising in the context of utilizing MnO_2 samples for fabricating electrodes in supercapacitor devices. However, MnO_2 -mw sample demonstrates higher power and energy densities as compared to MnO_2 -ref sample. Also the decrease in energy density with increasing power density is marginal for MnO_2 -mw sample as compared to MnO_2 -ref sample. The key to the superior performance of MnO_2 -mw sample is the availability of large amount of inner surface in the form of

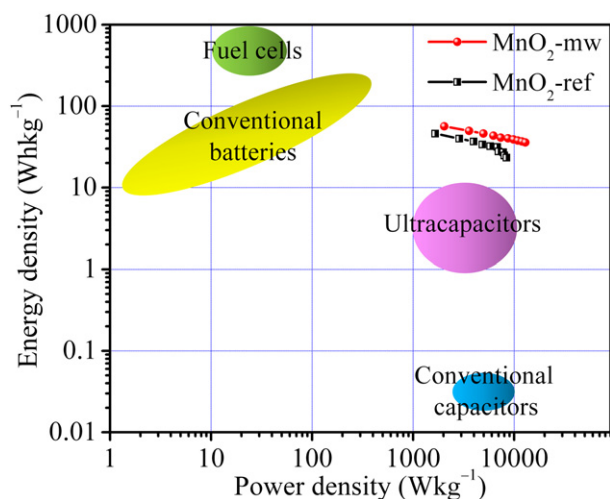


Fig. 9. The power density versus energy density of MnO_2 -ref and MnO_2 -mw samples in a Ragone plot for fuel cells, conventional batteries, conventional capacitors, and normal ultracapacitors [48].

curved MnO_2 nanosheets. Further, it is possible to improve the overall supercapacitance performance of MnO_2 -mw sample by employing ionic liquid electrolytes.

In summary, microwave mediated synthesis is a versatile approach to prepare hierarchically porous MnO_2 with better surface and bulk properties for high performance supercapacitor applications.

4. Conclusions

In this work, we have demonstrated the characteristic better surface properties like uniform surface morphology, high surface area, pore volume and bimodal pore size distribution of α - MnO_2 samples synthesized under microwave assisted method as compared to conventional-reflux methods. The electrochemical studies of the α - MnO_2 samples show explicit influence of surface properties on the pseudocapacitance performance. The CV studies show considerably improved high rate pseudocapacitance of the microwave synthesized α - MnO_2 sample over the conventional-reflux synthesized α - MnO_2 sample. This is attributed to facile electrolyte penetration, lowered ion diffusion resistance and better Faradaic utilization of the porous flower like arranged structures made up of layered rippled-surface flakes. The CP study under various current density conditions shows better I–V response, improved electrochemical reversibility, high retention at elevated current density condition, small IR drops and superior coulombic efficiency of the microwave synthesized α - MnO_2 sample. Further, the EIS analysis shows lower ESR value, high power performance, excellent rate as well as frequency response, and lower response time of the microwave synthesized α - MnO_2 sample. The Ragone plot ascertains better power and energy densities of microwave synthesized α - MnO_2 sample as compared to the conventional-reflux synthesized α - MnO_2 sample. This study illustrates that the microwave synthesis approach can have wider implications in fine-tuning surface properties of oxide materials for energy storage applications.

Acknowledgments

The authors acknowledge and thank MNRE and DRDO, New Delhi, for generous financial support. The instrumental facilities established under the FIST Scheme of SERC division of DST, Ministry of Science and Technology, New Delhi, have been very helpful to carry out this work. We also thank Mr. A. Narayanan and Mrs. S. Srividya for BET, TGA and XRD measurements.

Appendix A. Supplementary material

Supplementary material associated with this article can be found, in the online version, at doi:10.1016/j.jpowsour.2012.04.104.

References

- [1] J.A. Turner, Science 285 (1999) 687–689;
- [2] D.R. Rolison, J.W. Long, J.C. Lytle, A.E. Fischer, C.P. Rhodes, T.M. McEvoy, M.E. Bourg, A.M. Lubers, Chem. Soc. Rev. 38 (2009) 226–252;
- [3] C. Liu, F. Li, L.-P. Ma, H.-M. Cheng, Adv. Mater. 22 (2010) E28–E62.
- [4] B.E. Conway, Electrochemical Supercapacitors: Scientific Fundamentals and Technological Applications, Kluwer Academic/Plenum Publishers, New York, 1999;
- [5] P.J. Hall, M. Mirzaei, S.I. Fletcher, F.B. Sillars, A.J.R. Rennie, G.O. Shitta-Bey, G. Wilson, A. Cruden, R. Carter, Energy Environ. Sci. 3 (2010) 1238–1251;
- [6] X. Zhao, B.M. Sánchez, P.J. Dobson, P.S. Grant, Nanoscale 3 (2011) 839–855.
- [7] R. Kötz, M. Carlen, Electrochim. Acta 45 (2000) 2483–2498.
- [8] J.R. Miller, A.F. Burke, Electrochem. Soc. Interface (2008) 53–57.
- [9] P. Simon, Y. Gogotsi, Nat. Mater. 7 (2008) 845–854.
- [10] L. Hu, J.W. Choi, Y. Yang, S. Jeong, F.L. Mantia, L.-F. Cui, Y. Cui, Proc. Natl. Acad. Sci. USA. 106 (2009) 21490–21494.

- [7] D. Pech, M. Brunet, H. Durou, P. Huang, V. Mochalin, Y. Gogotsi, P.-L. Taberna, P. Simon, *Nat. Nanotechnol.* 5 (2010) 651–654.
- [8] R. Liu, J. Duay, S.B. Lee, *Chem. Commun.* 47 (2011) 1384–1404.
- [9] (a) K. Naoi, P. Simon, *Electrochem. Soc. Interface* (2008) 34–37;
(b) M.S. Whittingham, *MRS Bull.* 33 (2008) 411–419;
(c) A. Davies, A. Yu, *Can. J. Chem. Eng.* 9999 (2011) 1–16;
(d) C.D. Lokhande, D.P. Dubal, O.-S. Joo, *Curr. Appl. Phys.* 11 (2011) 255–270.
- [10] W. Deng, X. Ji, Q. Chen, C.E. Banks, *RSC Adv.* 1 (2011) 1171–1178.
- [11] G. Wang, L. Zhang, J. Zhang, *Chem. Soc. Rev.* 41 (2012) 797–828.
- [12] (a) C. Lin, J.A. Ritter, B.N. Popov, *J. Electrochem. Soc.* 146 (1999) 3155–3160;
(b) C.-C. Hu, W.-C. Chen, K.-H. Chang, *J. Electrochem. Soc.* 151 (2004) A281–A290;
(c) C.-C. Hu, K.-H. Chang, M.-C. Lin, Y.-T. Wu, *Nano Lett.* 6 (2006) 2690–2695.
- [13] S.L. Brock, N. Duan, Z.R. Tian, O. Giraldo, H. Zhou, S.L. Suib, *Chem. Mater.* 10 (1998) 2619–2628.
- [14] D. Bélanger, T. Brousse, J.W. Long, *Electrochem. Soc. Interface* (2008) 49–52.
- [15] (a) W. Wei, X. Cui, W. Chen, D.G. Ivey, *Chem. Soc. Rev.* 40 (2011) 1697–1721;
(b) H. Jiang, L. Yang, C. Li, C. Yan, P.S. Lee, J. Ma, *Energy Environ. Sci.* 4 (2011) 1813–1819;
(c) Y.-T. Wang, A.-H. Lu, H.-L. Zhang, W.-C. Li, *J. Phys. Chem. C* 115 (2011) 5413–5421;
(d) A.J. Roberts, R.C.T. Slade, *Energy Environ. Sci.* 4 (2011) 2813–2817.
- [16] S. Devaraj, N. Munichandraiah, *J. Phys. Chem. C* 112 (2008) 4406–4417.
- [17] B.E. Conway, V. Birss, J. Wojtowicz, *J. Power Sources* 66 (1997) 1–14.
- [18] M. Toupin, T. Brousse, D. Bélanger, *Chem. Mater.* 16 (2004) 3184–3190.
- [19] C. Xu, C. Wei, B. Li, F. Kang, Z. Guan, *J. Power Sources* 196 (2011) 7854–7859.
- [20] X. Lang, A. Hirata, T. Fujita, M. Chen, *Nat. Nanotech.* 6 (2011) 232–236.
- [21] X. Wang, Y. Li, *J. Am. Chem. Soc.* 124 (2002) 2880–2881.
- [22] M. Xu, L. Kong, W. Zhou, H. Li, *J. Phys. Chem. C* 111 (2007) 19141–19147.
- [23] P. Ragupathy, H.N. Vasan, N. Munichandraiah, *J. Electrochem. Soc.* 155 (2008) A34–A40.
- [24] W. Wei, X. Cui, W. Chen, D.G. Ivey, *J. Phys. Chem. C* 112 (2008) 15075–15083.
- [25] C. Xu, Y. Zhao, G. Yang, F. Li, H. Li, *Chem. Commun.* (2009) 7575–7577.
- [26] S. Chen, J. Zhu, Q. Han, Z. Zheng, Y. Yang, X. Wang, *Cryst. Growth Des.* 9 (2009) 4356–4361.
- [27] X. Lu, D. Zheng, T. Zhai, Z. Liu, Y. Huang, S. Xie, Y. Tong, *Energy Environ. Sci.* 4 (2011) 2915–2921.
- [28] G. Qiu, H. Huang, S. Dharmarathna, E. Benbow, L. Stafford, S.L. Suib, *Chem. Mater.* 23 (2011) 3892–3901.
- [29] C. Yuan, L. Hou, L. Yang, D. Li, L. Shen, F. Zhang, X. Zhang, *J. Mater. Chem.* 21 (2011) 16035–16041.
- [30] V. Subramanian, H. Zhu, R. Vajtai, P.M. Ajayan, B. Wei, *J. Phys. Chem. B* 109 (2005) 20207–20214.
- [31] H. Chen, X. Dong, J. Shi, J. Zhao, Z. Hua, J. Gao, M. Ruan, D. Yan, *J. Mater. Chem.* 17 (2007) 855–860.
- [32] A.L.M. Reddy, M.M. Shaijumon, S.R. Gowda, P.M. Ajayan, *J. Phys. Chem. C* 114 (2010) 658–663.
- [33] (a) T. Xue, C.-L. Xu, D.-D. Zhao, X.-H. Li, H.-L. Li, *J. Power Sources* 164 (2007) 953–958;
(b) W. Yan, T. Ayvazian, J. Kim, Y. Liu, K.C. Donavan, W. Xing, Y. Yang, J.C. Hemminger, R.M. Penner, *ACS Nano* 5 (2011) 8275–8287;
(c) C.-L. Ho, M.-S. Wu, *J. Phys. Chem. C* 115 (2011) 22068–22074.
- [34] (a) R. Liu, S.B. Lee, *J. Am. Chem. Soc.* 130 (2008) 2942–2943;
(b) Y. Hou, Y. Cheng, T. Hobson, J. Liu, *Nano Lett.* 10 (2010) 2727–2733.
- [35] G.-R. Li, Z.-P. Feng, Y.-N. Ou, D. Wu, R. Fu, Y.-X. Tong, *Langmuir* 26 (2010) 2209–2213.
- [36] Y. Peng, Z. Chen, J. Wen, Q. Xiao, D. Weng, S. He, H. Geng, Y. Lu, *Nano Res.* 4 (2011) 216–225.
- [37] (a) K.-W. Nam, C.-W. Lee, X.-Q. Yang, B.W. Cho, W.-S. Yoon, K.-B. Kim, *J. Power Sources* 188 (2009) 323–331;
(b) L. Hu, W. Chen, X. Xie, N. Liu, Y. Yang, H. Wu, Y. Yao, M. Pasta, H.N. Alshareef, Y. Cui, *ACS Nano* 5 (2011) 8904–8913.
- [38] (a) G. Yu, L. Hu, M. Vosgueritchian, H. Wang, X. Xie, J.R. McDonough, X. Cui, Y. Cui, Z. Bao, *Nano Lett.* 11 (2011) 2905–2911;
(b) Z. Fan, J. Yan, T. Wei, L. Zhi, G. Ning, T. Li, F. Wei, *Adv. Funct. Mater.* 21 (2011) 2366–2375;
(c) H. Lee, J. Kang, M.S. Cho, J.-B. Choi, Y. Lee, *J. Mater. Chem.* 21 (2011) 18215–18219.
- [39] (a) G.A. Tompsett, W.C. Conner, K.S. Yngvesson, *ChemPhysChem* 7 (2006) 296–319;
(b) S.H. Jung, T. Jin, Y.K. Hwang, J.-S. Chang, *Chem. Eur. J.* 13 (2007) 4410–4417;
(c) I. Bilecka, M. Niederberger, *Nanoscale* 2 (2010) 1358–1374.
- [40] E.K. Nyutu, C.-H. Chen, S. Sithambaram, V.M.B. Crisostomo, S.L. Suib, *J. Phys. Chem. C* 112 (2008) 6786–6793.
- [41] H. Huang, S. Sithambaram, C.-H. Chen, C.K. Kithongo, L. Xu, A. Iyer, H.F. Garces, S.L. Suib, *Chem. Mater.* 22 (2010) 3664–3669.
- [42] M. Zhou, X. Zhang, J. Wei, S. Zhao, L. Wang, B. Feng, *J. Phys. Chem. C* 115 (2011) 1398–1402.
- [43] B. Ming, J. Li, F. Kang, G. Pang, Y. Zhang, L. Chen, J. Xu, X. Wang, *J. Power Sources* 198 (2012) 428–431.
- [44] J. Post, *Proc. Natl. Acad. Sci. USA* 96 (1999) 3447–3454.
- [45] D. Zhai, B. Li, C. Xu, H. Du, Y. He, C. Wei, F. Kang, *J. Power Sources* 196 (2011) 7860–7867.
- [46] J. Ge, L. Zhuo, F. Yang, B. Tang, L. Wu, C. Tung, *J. Phys. Chem. B* 110 (2006) 17854–17859.
- [47] J. Luo, H.T. Zhu, J.K. Liang, G.H. Rao, J.B. Li, Z.M. Du, *J. Phys. Chem. C* 114 (2010) 8782–8786.
- [48] O. Ghodbane, J.-L. Pascal, B. Fraisse, F. Favier, *ACS Appl. Mater. Interfaces* 2 (2010) 3493–3505.
- [49] S.K. Meher, P. Justin, G. Ranga Rao, *ACS Appl. Mater. Interfaces* 3 (2011) 2063–2073.
- [50] (a) H. Köfgen, M. Antonietti, *Angew. Chem. Int. Ed.* 44 (2005) 5576–5591;
(b) J.K. Bishop, C.E. Wilmer, S. Soh, B.A. Grzybowski, *Small* 5 (2009) 1600–1630;
(c) R.-Q. Song, H. Cölfen, *CrystEngComm* 13 (2011) 1249–1276.
- [51] (a) G.M. Whitesides, M. Boncheva, *Proc. Natl. Acad. Sci. USA* 8 (2002) 4769–4774;
(b) G.A. Ozin, K. Hou, B.V. Lotsch, L. Cademartiri, D.P. Puzzo, F. Scotognella, A. Ghadimi, J. Thomson, *Mater. Today* 12 (2009) 12–23;
(c) M. Grzelczak, J. Vermant, E.M. Furst, L.M. Liz-Marzán, *ACS Nano* 4 (2010) 3591–3605.
- [52] D. Zheng, S. Sun, W. Fan, H. Yu, C. Fan, G. Cao, Z. Yin, X. Song, *J. Phys. Chem. B* 109 (2005) 16439–16443.
- [53] (a) S.T. Bromley, I.P.R. Moreira, K.M. Neyman, F. Illas, *Chem. Soc. Rev.* 38 (2009) 2657–2670;
(b) P. Yu, X. Zhang, D. Wang, L. Wang, Y. Ma, *Cryst. Growth Des.* 9 (2009) 528–533;
(c) G.R. Patzke, Y. Zhou, R. Kontic, F. Conrad, *Angew. Chem. Int. Ed.* 50 (2011) 826–859.
- [54] F. Rouquerol, J. Rouquerol, K. Sing, *Adsorption by Powders and Porous Solids*, Academic Press, London, 1999.
- [55] S.K. Meher, P. Justin, G. Ranga Rao, *Nanoscale* 3 (2011) 683–692.
- [56] M.D. Stoller, R.S. Ruoff, *Energy Environ. Sci.* 3 (2010) 1294–1301.
- [57] (a) M. Toupin, T. Brousse, D. Bélanger, *Chem. Mater.* 14 (2002) 3946–3952;
(b) S. Wen, J.-W. Lee, I.-H. Yeo, J. Park, S. Mho, *Electrochim. Acta* 50 (2004) 849–855.
- [58] (a) S.-C. Pang, M.A. Anderson, T.W. Chapman, *J. Electrochem. Soc.* 147 (2000) 444–450;
(b) S.-L. Kuo, N.-L. Wu, *J. Electrochem. Soc.* 153 (2006) A1317–A1324;
(c) P.K. Nayak, N. Munichandraiah, *J. Electrochem. Soc.* 158 (2011) A585–A591.
- [59] W.G. Pell, B.E. Conway, *J. Electroanal. Chem.* 500 (2001) 121–133.
- [60] S.K. Meher, P. Justin, G. Ranga Rao, *Electrochim. Acta* 55 (2010) 8388–8396.
- [61] O. Ghodbane, J.-L. Pascal, F. Favier, *ACS Appl. Mater. Interfaces* 1 (2009) 1130–1139.
- [62] G.-Q. Zhang, S.-T. Zhang, *J. Appl. Electrochem.* 39 (2009) 1033–1038.
- [63] P. Justin, S.K. Meher, G. Ranga Rao, *J. Phys. Chem. C* 114 (2010) 5203–5210.
- [64] V. Srinivasan, J.W. Weidner, *J. Power Sources* 108 (2002) 15–20.
- [65] S.K. Meher, G. Ranga Rao, *J. Phys. Chem. C* 115 (2011) 15646–15654.
- [66] S.K. Meher, G. Ranga Rao, *J. Phys. Chem. C* 115 (2011) 25543–25556.
- [67] J. Chmiola, G. Yushin, Y. Gogotsi, C. Portet, P. Simon, P.L. Taberna, *Science* 313 (2006) 1760–1763.
- [68] B.E. Conway, W.G. Pell, *J. Power Sources* 105 (2002) 169–181.
- [69] H. Zhang, G. Cao, Y. Yang, Z. Gu, *J. Electrochem. Soc.* 155 (2008) K19–K22.
- [70] F.-L. Zheng, G.-R. Li, Y.-N. Ou, Z.-L. Wang, C.-Y. Su, Y.-X. Tong, *Chem. Commun.* 46 (2010) 5021–5023.
- [71] D.-W. Wang, F. Li, M. Liu, G.-Q. Lu, H.-M. Cheng, *Angew. Chem. Int. Ed.* 47 (2008) 373–376.
- [72] (a) W.G. Pell, B.E. Conway, N. Marincic, *J. Electroanal. Chem.* 491 (2000) 9–21;
(b) Y.-C. Hsieh, K.-T. Lee, Y.-P. Lin, N.-L. Wu, S.W. Donne, *J. Power Sources* 177 (2008) 660–664.
- [73] A.A.F. Grupioni, T.A.F. Lassali, *J. Electrochem. Soc.* 148 (2001) A1015–A1022.
- [74] W. Sugimoto, H. Iwata, K. Yokoshima, Y. Murakami, Y. Takasu, *J. Phys. Chem. B* 109 (2005) 7330–7338.
- [75] C.-C. Hu, K.-H. Chang, T.-Y. Hsu, *J. Electrochem. Soc.* 155 (2008) F196–F200.
- [76] J. Zhang, J. Jiang, X.S. Zhao, *J. Phys. Chem. C* 115 (2011) 6448–6454.
- [77] (a) R. de Levie, *Electrochim. Acta* 8 (1963) 751–780;
(b) H.-K. Song, Y.-H. Jung, K.-H. Lee, L.H. Dao, *Electrochim. Acta* 44 (1999) 3513–3519;
(c) H.-K. Song, H.-Y. Hwang, K.-H. Lee, L.H. Dao, *Electrochim. Acta* 45 (2000) 2241–2257.
- [78] (a) J. Li, F. Gao, *J. Power Sources* 194 (2009) 1184–1193;
(b) H. Wang, H.S. Casalongue, Y. Liang, H. Dai, *J. Am. Chem. Soc.* 132 (2010) 7472–7477.
- [79] B.C. Jones, A.F. Hollenkamp, S.W. Donne, *J. Electrochem. Soc.* 157 (2010) A551–A557.